Optics Letters

Proposal for achieving in-plane magnetic mirrors by silicon photonic crystals

You Zhou,† Xin-Tao He,† Fu-Li Zhao, and Jian-Wen Dong*

State Key Laboratory of Optoelectronic Materials and Technologies & School of Physics, Sun Yat-sen University, Guangzhou 510275, China
**Corresponding author: dongjwen@mail.sysu.edu.cn*

Received 22 February 2016; revised 4 April 2016; accepted 9 April 2016; posted 11 April 2016 (Doc. ID 259730); published 5 May 2016

Magnetic mirrors exhibit predominant physical characteristics such as high surface impedance and strong near-field enhancement. However, there is no way to implement these materials on a silicon lab chip. Here, we propose a scheme for an in-plane magnetic mirror in a silicon-based photonic crystal with a high-impedance surface, in contrast to the previous electric mirrors with low surface impedance. A tortuous bending waveguide with zero-index core and magnetic mirror walls is designed that exhibits high transmission and zero phase change at the waveguide exit. This type of magnetic mirror opens the door to exploring the physics of high-impedance surfaces and applications in integrated photonics.

OCIS codes: (160.5298) Photonic crystals; (290.4020) Mie theory; (160.3918) Metamaterials.

http://dx.doi.org/10.1364/OL.41.002209

Metals have long been used as reflectors in optoelectronic devices. High conductivity of metal surfaces, which formulate the reversed phase of electric fields generated upon reflection, gives rise to the node of overall tangential electric field within a quarter wavelength near the surface. This leads to problems in miniature devices such as antennas or active layers. Another kind of extraordinary mirror, the so-called magnetic mirror, can produce in-phase reflected waves and tends to have promising applications. The magnetic mirror is characterized by large effective impedance and requires artificial composites to mimic the bulk electromagnetic property. The first high-impedance surface was proposed in microwaves by the building blocks of metal plates or corrugated grooves [1]. Later, various metallic inclusions were proposed, such as fishnet strips, Hilbert curves, and gold-coated carbon nanotubes [2–4]. Relevant studies have found the potential for improving miniature antenna performance [5–8] or enhancing light absorption in active layers [9,10]. In the optical regime, metallic fishnet-scale strips were first employed to achieve a magnetic mirror with unsatisfactory reflectivity and reflection phase change due to inevitable ohmic loss in the metallic components [11]. All-dielectric structures then become necessary to obtain a high-performance magnetic mirror. So far, all-dielectric resonators such as cross-shaped a-Si [12] and cubic Te [13,14] have been introduced to realize optical magnetic mirrors (OMMs), but they are particularly applied for normal incidence to the device plane.

On the other hand, all-dielectric metamaterial can serve as a promising candidate and an alternative way for tailoring the electric and magnetic resonances at optical frequencies with low absorption loss limits. Properly designing the size, permittivity, and geometry of dielectric unit cells allows the control of electric and magnetic dipole resonances. By overlapping electric and magnetic dipole resonance spectrally, impedance-matched Huygens surfaces have been proposed by using all-dielectric nanodisks [15,16]. Recently, the generalized Brewster effect is also achieved with angle-suppressed scattering from electric and magnetic dipole interference [17]. Here we propose a strategy to achieve in-plane magnetic mirrors from all-dielectric photonic crystals (PCs). One advantage of PC-based magnetic mirrors is due to the fact that the mirrors could be constructed by vertical growth of rod arrays on the same supporting substrate of other photonic-integrated circuit components. In principle, a PC with a complete photonic bandgap provides the frequency range to expel disallowed modes [18–20], acting as high reflectors. Extensive investigations have revealed its applications for guiding wave [21] and resonant cavities [22,23]. Rather than the reflection phase-shift change, reflection amplitude in PC-based integrated devices has been the focus of previous literature. Until very recently, studies on reflection phase and surface impedance have revealed the existing condition on the edge state in the interface of two photonic-bandgap materials [24], and also revealed the edge states in relation to the nontrivial Zak phase in both photonic and phononic crystals [25–27]. From the magnetic mirror point of view, it is not only to ensure strong reflection but also to gain the near-zero reflection phase shift at the PC surface, equivalent to the realization of a high-reflective surface with large impedance. Whether or not PC-based magnetic mirrors can exist is still an open question.

In this Letter, we propose a kind of in-plane magnetic mirror in a silicon-based PC. The high-impedance feature is derived when the working frequency is near the photonic band edge, leading to the enhancement on the electric field within the quarter wavelength distance of the PC surface. By virtue of their high-impedance characteristics, magnetic-mirror PCs can be applied as high-impedance boundary walls to achieve high transmission and zero-phase delay in zero-index waveguides,

even when light experiences sharp turns in the waveguide channel.

The in-plane magnetic mirror can be modeled as a 2D array of silicon rods placed in air background. The lattice constant is a. The rod radius is $R = 0.331a$, and the dielectric constant of $\epsilon = 12$. Such a set of parameters brings a complete bandgap from 0.221 to 0.273 c/a in the whole momentum space, allowing strong electromagnetic reflections. At the frequency near 0.273 c/a, the PC can exhibit a collective feature of high impedance (quantitative results will be shown later). A schematic picture is shown in Fig. 1(a), indicating that both the incident and reflected wave (yellow arrows) yield the same phase shift in the electric field (red) while the reversed phase shift in the magnetic field (green arrows) at the surface of magnetic-mirror PC occurs. Instructive interferences of the electric field between the incident and reflected waves will enhance the amplitude of electric field ($|E|$) within a quarter wavelength distance near the surface, while the amplitude of magnetic field ($|H|$) is suppressed due to destructive interference. This is verified by COMSOL calculations, as shown in Figs. 1(b) and 1(c). The electric field near the topmost cylinders (gray circles) reaches the maximum value (inside white dash), while the magnetic field is minimum in the same region. This is consistent with the case when the magnetic-mirror PC is replaced by an ideal perfect magnetic conductor (PMC) [Figs. 1(d)–1(f)]. For comparison, a counterexample of a perfect electric conductor (PEC) is also plotted in Figs. 1(g)–1(i), revealing the suppression of $|E|$ while the enhancement of $|H|$ is nearly the PEC surface.

Figure 2(a) illustrates the projected band structure along x direction with transverse magnetic polarization (electric field along the rod's axis). The pink marks the passband, while the white denotes the bandgap. It is found that there is a large

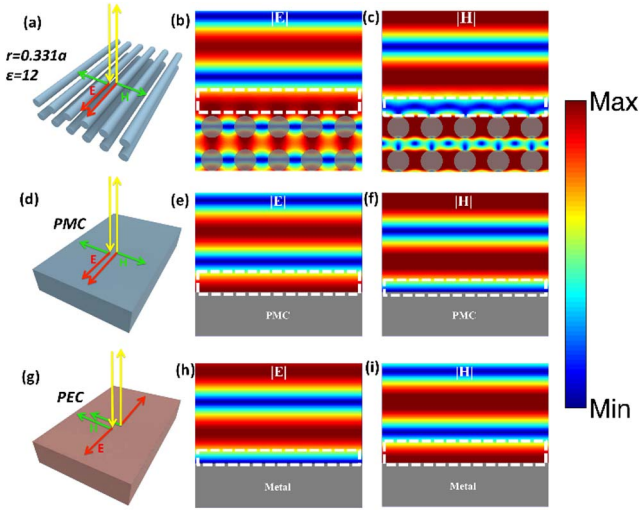

Fig. 1. (a) Schematic diagram of optical all-dielectric magnetic mirror constructed by two-dimensional PCs. There is the same phase shift of the electric fields (red) between the incident and reflected waves (yellow), while the opposite occurs with the magnetic fields (green). (b) Electric fields and (c) magnetic fields near the surface of the magnetic mirror. (d)–(f) The same case when the magnetic-mirror PC is replaced by an ideal perfect magnetic conductor (PMC). (g)–(i) Comparison when the reflection plane is the lossless metal mirror, mimicking perfect electric conductor (PEC).

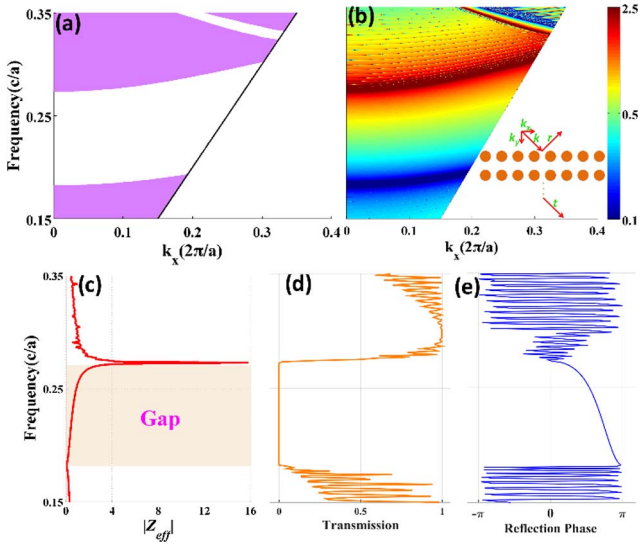

Fig. 2. (a) Projected band structure along x direction for the square PC with $R = 0.331a$ and $\epsilon = 12$. (b) Distribution of the effective impedance $|Z_{\text{eff}}(\omega, k_x)|$ calculated by 30 layers of silicon rods. (c) $|Z_{\text{eff}}(\omega, k_x)|$ for normal incidence ($k_x = 0$). (d) The transmission spectrum and (e) the reflection phase for normal incidence.

gap between 0.182 and 0.273 c/a at $k_x = 0$, indicating strong reflection within this frequency region at normal incidence. However, the key point of the magnetic mirror is to investigate the effective impedance within the bandgap. Following the well-established retrieval methods from scattering parameters [28,29], the effective impedance $Z_{\text{eff}}(\omega, k_x)$ is calculated by full-wave simulations; the results are shown in Fig. 2(b). In principle, a semi-infinite stack of periodic layers should be employed in the retrieval process, but the value of $Z_{\text{eff}}(\omega, k_x)$ inside the bandgap can converge to a constant when the number of layers is as many as 30. As illustration of the inset of Fig. 2(b), a plane wave is incident on the top, and periodic conditions are applied along x direction for each wave vector and angle of incidence. The Z_{eff} (ω, k_x) is obtained from the extracted reflection (r) and transmission (t) coefficients [25]

$$Z_{\text{eff}}(\omega, k_x) = \pm \frac{\sqrt{(1+r)^2 - t^2}}{\sqrt{(1-r)^2 - t^2} \cdot \sqrt{1 - k_x^2/k^2}}, \quad (1)$$

where k is the wave vector and k_x is its tangential component. The sign here ensures the condition for $\text{Re}(Z_{\text{eff}}(\omega, k_x)) > 0$. Figure 2(b) shows the magnitude of $Z_{\text{eff}}(\omega, k_x)$ above the light cone, with the same $\omega - k$ diagram as the projected band structure. The color bar is presented in logarithmic scale in order to distinguish the distributions of $|Z_{\text{eff}}(\omega, k_x)|$. The dark red strip with maximum value of $|Z_{\text{eff}}(\omega, k_x)|$ is near the upper band edge, while the dark blue strip is near the lower band edge, implying that the magnetic mirror and the electric mirror can be realized near such frequency regimes, respectively. The glitches at a higher passband arise from Fabry–Perot resonance inside the passband. To clarify the value of effective impedance, Fig. 2(c) plots the variation of $|Z_{\text{eff}}(\omega, k_x)|$ as a function of the frequency for normal incidence ($k_x = 0$). It is found that the effective impedance is monotonically increasing inside the bandgap (shaded region). A peak occurs at the frequency of 0.273 c/a with the maximum value of ~16, while

$|Z_{\text{eff}}(\omega, k_x)|$ goes to zero at the first band edge of 0.182 c/a. For the frequency of the upper pass band, a few oscillations are found due to Fabry–Perot resonance, which is also verified from the transmission spectrum illustrated in Fig. 2(d). The oscillations in transmission spectrum are derived from inter-scattering between rods, of which the periods are highly dependent on the number of rods stacked along the y direction. The calculated reflection phase (φ) in Fig. 2(e) manifests a monotonic decrease of $|\varphi|$ from π to 0 at the two band edges as the frequency increases. It attests to the distributions of $|Z_{\text{eff}}(\omega, k_x)|$, which prescribes a small reflection phase in response to large surface impedance.

Next, we will show that OMM PCs can be utilized as high-impedance boundary walls. Recently, the electromagnetic behaviors such as invisibility cloak and sharp-turn energy tunneling have been demonstrated in the microwave waveguide with the high impedance surface cladding and the zero-index core [30–33]. In those behaviors, the zero-index core can be constructed by an all-dielectric PC with triplet accidentally degenerates conical dispersion at Γ point in both the microwave and optical frequency regime. However, a zero-index PC is not sufficient for a whole waveguide system. When the electromagnetic wave propagates through the waveguide with the core of a zero-index PC, one should have perfect-magnetic-conductor boundaries as the magnetic-reflection wall in order to mimic the infinite periodicity and to ensure high transmission and unchanged output transverse-magnetic polarized wavefronts. This is easy to accomplish by delicate design on a metal plane and using the mature printed circuit board technique in microwave, but it cannot scale into the telecommunication regime, as metal is seriously dispersive and lossy. The solution is to replace it with the all-dielectric magnetic-mirror PC because of its high impedance characteristics.

As a representative example, we assume the lattice constant of the zero-index silicon PC to be $a_1 = 2a$, so that the zero-index band is near the high-impedance frequency of 0.273 c/a in the magnetic-mirror PC. The rod radius of the zero-index PC is $R_1 = 0.4048a$. Figure 3(a) illustrates the effective permittivity and permeability, indicating that the working frequency for the zero-index is well designed at 0.273 c/a. In this way, one can construct a full PC-based waveguide channel with a zero-index core and high-impedance cladding, as shown in Fig. 3(c). Both the core and cladding have 10 rows of rods along the y direction. When the working frequency is at 0.273 c/a, it is observed that the electric field is almost in-phase inside the zero-index PC, while the exit wave is of high transmittance and almost keeps the plane wave profiles. It is also found that the electric fields experience strong reflection upon the high-impedance boundary wall with little penetration into the OMM at both sides. Note that the slightly distorted plane wavefront in both the incident and exit air region is due to multiple interferences at the interface of the OMM and the zero-index PC. Control calculation is calculated in Fig. 3(b) for the case of an ideal PMC boundary, showing the similar behavior as those in Fig. 3(c). This verifies the fact that the magnetic-mirror PC can play a role as the PMC boundary. One prominent advantage of such substitution is that all-dielectric materials in a zero-index and magnetic-mirror PCs may benefit to low-loss photonic integral circuits at optical frequencies.

Next, we will implement the magnetic-mirror PC into the zero-index waveguide with tortuous transmission paths, in order to further illustrate the nontrivial OMM behavior. We take the 180° bend waveguide as an example. The simulation results are in Figs. 4(a) and 4(b) for the cases of an ideal perfect magnetic mirror and a PC-based OMM, showing the equivalence to each other at the frequency of 0.273 c/a. To completely investigate the high impedance feature, Fig. 4(c) shows the variation of $|Z_{\text{eff}}(\omega, k_x)|$ as a function of the rod radius in the cladding PC. Here, we fix the working frequency at 0.273 c/a and restrict the radius with the values that guarantee the frequency within the bandgap. When the radius reduces from 0.331a, the value of $|Z_{\text{eff}}(\omega, k_x)|$ decreases monotonically. This is because the photonic band structure [similar in Fig. 2(a)] moves to higher frequency as the radius reduces, leading to the notion that the working frequency is at the regime of the low-impedance mirror of the magnetic-mirror PC. As a result, the transmission of the bending waveguide will become low and the plane wavefront will be severely distorted if the rod radius of the cladding PC changes away from 0.331a. This is verified as a typical example at $R = 0.3a$, as shown in

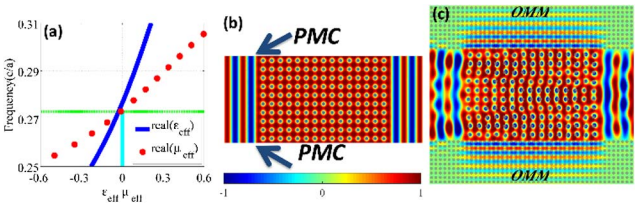

Fig. 3. (a) Effective permittivity (ϵ_{eff}) and permeability (μ_{eff}) around the zero-index point. Note that ϵ_{eff} and μ_{eff} approach zero simultaneously at the frequency of 0.273 c/a. (b) The E_z field pattern for the straight zero-index core waveguide sandwiched by the ideal PMC boundaries. (c) Same as (b) except replacing the ideal PMC by an optical magnetic mirror (OMM).

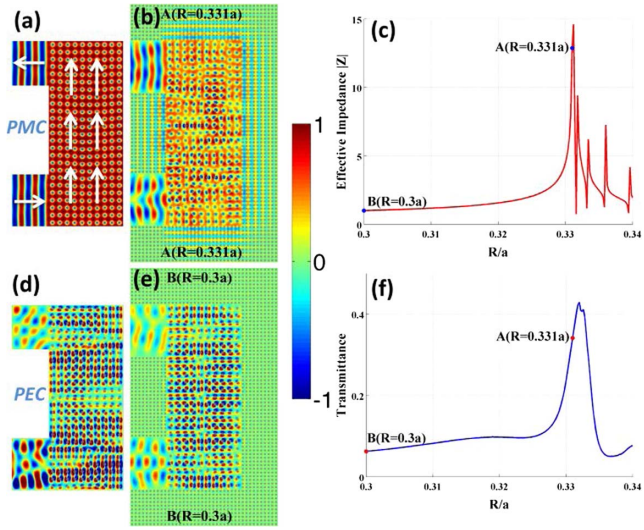

Fig. 4. Tortuous bending waveguide with the central core of zero-index PC and the side wall of either (a) the conceptual perfectly magnetic mirror or (b) artificial all-dielectric magnetic mirror. (c) The variation of $|Z_{\text{eff}}(\omega, k_x)|$ in the cladding PC when the working frequency is 0.273 c/a. (d) and (e) The E_z field pattern for boundary walls with (d) the ideal PEC and (e) electric-mirror PC with $R = 0.3a$. (f) Transmittance from the channel exit.

Fig. 4(e), sharing similar features as the case of perfect electric mirror [Fig. 4(d)]. Most of the energy experiences strong reflection back to the incident port, but is still confined inside the zero-index core. Note that the working frequency falls into the passband and the oscillations appear due to the Fabry–Perot resonance when the radius is larger than 0.331a.

To quantitatively measure the output from the bend waveguide, Fig. 4(f) shows the transmitted energy from the exit port as a function of the radius of the cladding PC. The distribution trends of the transmission and $|Z_{\text{eff}}(\omega, k_x)|$ are well consistent with each other. Figure 4(f) also implies that the output energy from the magnetic-mirror cladding (point A) is more than five times that from the electric-mirror cladding (point B). This is because the E_z field remains in-phase after bouncing off the high-impedance surface, resulting in uniform energy flow and high transmittance through the waveguide. However, the E_z field becomes out-of-phase when reflecting off the electric-mirror boundaries, leading to destructive interferences and weak flow of energy. Note that the transmittance in Fig. 4(f) is still high, even for the point $R = 0.332a$, with low effective impedance. This mismatch comes from the finite size effect. When the sizes of both the magnetic-mirror and the zero-index PCs increase, the transmission peak should approach the point of 0.331a.

The general fabrication strategy of such 2D all-dielectric PC with zero-index properties has already been realized by alternating layers deposition, electron beam lithography (EBL), and reactive ion etching (RIE) [32]. Despite the narrow available ranges of rod diameter between the electric mirror and the magnetic mirror, the scalar difference in diameter is still within today's EBL resolution. Suppose the working wavelength is 1.55 μm: then the lattice constant is $a = 423$ nm. The corresponding diameters of the magnetic mirror and the electric mirror are 280 nm and 254 nm, respectively. Such a 26 nm size difference is essentially achievable from EBL with extremely precise alignment and stigmation adjustment.

In conclusion, we have proposed a scheme for an in-plane magnetic mirror in silicon-based PCs. High-impedance characteristics ensure the enhanced electric field within the quarter wavelength distance near the PC surface. High transmission and zero phase change in the zero-index waveguide are achieved when the magnetic-mirror PCs are applied as high-impedance walls. Along with the natural accessibility to the silicon industry, the proposed all-dielectric OMM is highly compatible with today's advanced nanofabrication technology, and it has benefits in exploring the physics of high-impedance surfaces and their applications in photonic integrated circuits.

†These authors contributed equally to this work.

Funding. National Natural Science Foundation of China (NSFC) (11522437, 11274397, J1103211); Guangdong Natural Science Funds for Distinguished Young Scholar (S2013050015694); Guangdong Special Support Program.

REFERENCES

1. D. Sievenpiper, L. Zhang, R. F. J. Broas, N. G. Alexopolous, and E. Yablonovitch, IEEE Trans. Microwave Theory Tech. **47**, 2059 (1999).
2. V. A. Fedotov, S. L. Prosvirnin, A. V. Rogacheva, and N. I. Zheludev, Appl. Phys. Lett. **88**, 091119 (2006).
3. J. McVay and N. Engteta, IEEE Microwave Wireless Compon. Lett. **14**, 130 (2004).
4. H. Rostami, Y. Abdi, and E. Arzi, Carbon **48**, 3659 (2010).
5. Y. Zhang, J. von Hagen, and W. Wiesbeck, Microwave Opt. Technol. Lett. **35**, 172 (2002).
6. D. Yan, Q. Gao, C. Wang, and N. Yuan, PIERS Online **1**, 695 (2005).
7. B.-I. Wu, H. Chen, J. A. Kong, and T. M. Grzegorczyk, J. Appl. Phys. **101**, 114913 (2007).
8. G. Haibo, W. Yueshan, L. Yichang, and X. Kang, in *IEEE International Conference on RFID-Technology and Applications (RFID-TA)* (IEEE, 2010), p. 61.
9. M. Esfandyarpour, E. C. Garnett, Y. Cui, M. D. McGehee, and M. L. Brongersma, Nat. Nanotechnol. **9**, 542 (2014).
10. H. Dotan, O. Kfir, E. Sharlin, O. Blanck, M. Gross, I. Dumchin, G. Ankonina, and A. Rothschild, Nat. Mater. **12**, 158 (2012).
11. A. S. Schwanecke, V. A. Fedotov, V. Khardikov, S. L. Prosvirnin, Y. Chen, and N. I. Zheludev, J. Opt. A **9**, L1 (2007).
12. Z. H. Jiang, S. Yun, L. Lin, D. Brocker, D. H. Werner, and T. S. Mayer, in *Proceedings of the 2012 IEEE International Symposium on Antennas and Propagation* (IEEE, 2012), p. 1.
13. J. C. Ginn, I. Brener, D. W. Peters, J. R. Wendt, J. O. Stevens, P. F. Hines, L. I. Basilio, L. K. Warne, J. F. Ihlefeld, P. G. Clem, and M. B. Sinclair, Phys. Rev. Lett. **108**, 097402 (2012).
14. S. Liu, M. B. Sinclair, T. S. Mahony, Y. C. Jun, S. Campione, J. Ginn, D. A. Bender, J. R. Wendt, J. F. Ihlefeld, P. G. Clem, J. B. Wright, and I. Brener, Optica **1**, 250 (2014).
15. M. Decker, I. Staude, M. Falkner, J. Dominguez, D. N. Neshev, I. Brener, T. Pertsch, and Y. S. Kivshar, Adv. Opt. Mater. **3**, 813 (2015).
16. Y. F. Yu, A. Y. Zhu, R. Paniagua-Domínguez, Y. H. Fu, B. Luk'yanchuk, and A. I. Kuznetsov, Laser Photon. Rev. **9**, 412 (2015).
17. R. Paniagua-Dominguez, Y. F. Yu, A. E. Miroschnichenko, L. A. Krivitsky, Y. H. Fu, V. Valuckas, L. Gonzaga, Y. T. Toh, A. Y. S. Kay, B. Luk'yanchuk, and A. I. Kuznetsov, Nat. Commun. **7**, 10362 (2016).
18. E. Yablonovitch, Phys. Rev. Lett. **58**, 2059 (1987).
19. S. John, Phys. Rev. Lett. **58**, 2486 (1987).
20. H. Wang, C. J. R. Sheppard, K. Ravi, S. T. Ho, and G. Vienne, Laser Photon. Rev. **6**, 354 (2012).
21. A. Mekis, J. C. Chen, I. Kurland, S. Fan, P. R. Villeneuve, and J. D. Joannopoulos, Phys. Rev. Lett. **77**, 3787 (1996).
22. J. D. Joannopoulos, P. R. Villeneuve, and S. Fan, Solid State Commun. **102**, 165 (1997).
23. J. D. Joannopoulos, R. D. Meade, and J. N. Winn, *Photonic Crystals: Molding the Flow of Light* (Princeton University, 1995).
24. J. W. Dong, J. Zeng, Q. F. Dai, and H. Z. Wang, "Universal condition for the existence of interface modes in the whole momentum space with arbitrary materials," arXiv:0801.4117 (2008).
25. X. Huang, M. Xiao, Z.-Q. Zhang, and C. T. Chan, Phys. Rev. B **90**, 075423 (2014).
26. M. Xiao, G. Ma, Z. Yang, P. Sheng, Z. Q. Zhang, and C. T. Chan, Nat. Phys. **11**, 240 (2015).
27. M. Xiao, Z. Q. Zhang, and C. T. Chan, Phys. Rev. X **4**, 021017 (2014).
28. D. R. Smith, D. C. Vier, T. Koschny, and C. M. Soukoulis, Phys. Rev. E **71**, 036617 (2005).
29. X. Chen, T. M. Grzegorczyk, B.-I. Wu, J. Pacheco, and J. A. Kong, Phys. Rev. E **70**, 016608 (2004).
30. X. Q. Huang, Y. Lai, Z. H. Hang, H. Zheng, and C. T. Chan, Nat. Mater. **10**, 582 (2011).
31. J. W. Dong, M. L. Chang, X. Q. Huang, Z. H. Hang, Z. C. Zhong, W. J. Chen, and C. T. Chan, Phys. Rev. Lett. **114**, 163901 (2015).
32. P. Moitra, Y. Yang, Z. Anderson, I. I. Kravchenko, D. P. Briggs, and J. Valentine, Nat. Photonics **7**, 791 (2013).
33. Y. Li, S. Kita, P. Munoz, O. Reshef, D. I. Vulis, M. Yin, M. Loncar, and E. Mazur, Nat. Photonics **9**, 738 (2015).